Journal of Materials Chemistry A

Accepted Manuscript

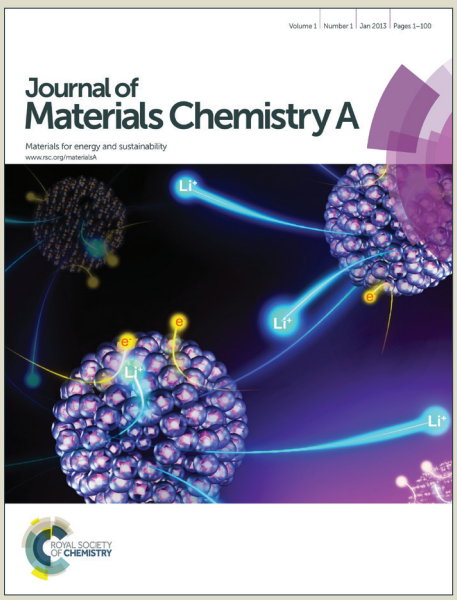

ROYAL SOCIETY OF CHEMISTRY

www.rsc.org/materialsA

Ab Initio DFT+U Analysis of Oxygen Transport in $LaCoO_3$: The Effect of Co^{3+} Magnetic States

Andrew M. Ritzmann,[1] Michele Pavone,[2] Ana B. Muñoz-García, [2] John A. Keith[3,†] and Emily A. Carter[3,4]*

[1]Department of Chemical and Biological Engineering, [2]Department of Chemical Sciences, University of Naples Federico II, Naples 80126, Italy [3]Deparment of Mechanical and Aerospace Engineering, [4]Program in Applied and Computational Mathematics, and Andlinger Center for Energy and the Environment, Princeton University, Princeton, NJ 08544-5263, United States

Keywords: Lanthanum cobaltite, $LaCoO_3$, Solid Oxide Fuel Cell, Oxygen Vacancy, Oxygen Diffusion

ABSTRACT:
Although solid oxide fuel cells (SOFCs) provide clean and efficient electricity generation, high operating temperatures ($T>800^oC$) limit their widespread use. Lowering operating temperatures ($600^oC<T<800^oC$) requires developing next-generation mixed ion-electron conducting (MIEC) cathodes that permit facile oxygen transport. One promising MIEC material, $La_{1-x}Sr_xCo_{1-y}Fe_yO_3$ (LSCF), can operate at intermediate temperatures, has a longer cell lifetime, and permits less expensive interconnect materials. However, the road to optimization of LSCF compositions for SOFC applications would benefit from fundamental, atomic-scale insight into how local chemical changes affect its oxygen ion conductivity. We provide this insight using *ab initio* density functional theory plus U (DFT+U) calculations to analyze the factors governing oxygen transport in the LSCF parent material $LaCoO_3$. We show that oxygen diffusion in $LaCoO_3$ depends strongly on the spin state of the Co^{3+} ions: in particular, low spin Co^{3+} promotes higher oxygen vacancy concentrations than other spin states. We also predict that different spin states of Co^{3+} significantly affect the oxygen ion migration barrier. Through electronic structure analysis, we uncover the fundamental details which govern oxygen diffusivity in $LaCoO_3$.

INTRODUCTION

Solid oxide fuel cells (SOFCs) can efficiently convert a variety of fuels into electricity, making them potentially useful for multiple, diverse energy applications.[1–5] Development of next-generation SOFCs requires finding solid state cathode materials capable of mixed oxygen ion and electron conduction (MIEC).[6] $LaCoO_3$ and its substituted forms ($La_{1-x}Sr_xCoO_3$, $La_{1-x}Sr_xFe_{1-y}Co_yO_3$) promisingly demonstrate facile oxygen transport.[7–10] However, insufficient atomic-level understanding of the physical and chemical properties of $LaCoO_3$ inhibits the rational design of $LaCoO_3$-based SOFC cathode materials. Most importantly, the relationship between magnetism and oxygen transport in $LaCoO_3$ remains largely unexplored.

Co^{3+} ions introduce complex magnetic behavior in $LaCoO_3$ by occupying octahedral sites surrounded by oxygen ions (the slight rhombohedral distortion is customarily neglected).[11] This crystal

field splits the *d* orbitals into a triply-degenerate set of t_{2g} orbitals below a doubly-degenerate set of e_g orbitals. Combining the crystal field splitting with the $3d^6$ valence configuration leads to three local spin states for Co^{3+}: low spin (LS, $t_{2g}^6e_g^0$), intermediate spin (IS, $t_{2g}^5e_g^1$), and high spin (HS, $t_{2g}^4e_g^2$). The IS state should display a strong Jahn-Teller (JT) distortion that breaks the degeneracy of the e_g orbitals. $LaCoO_3$ exhibits nonmagnetic behavior at low temperatures, so the Co^{3+} ions remain in the LS spin state below 90 K.[12,13] The material undergoes a nonmagnetic-to-paramagnetic transition below 100 K[14] and an insulator-to-metal transition around 500 K.[15–18] Disagreement arises regarding the spin state of the Co^{3+} ions above the onset of the first transition. Some X-ray diffraction experiments[19] suggest the existence of IS Co^{3+} ions while other soft X-ray absorption and circular dichroism experiments[20] indicate that a mixture of HS and LS Co^{3+} ions coexist. Another X-ray absorption study finds a continuous LS to IS transition around 90 K.[21] All of these interpretations are consistent with the observed magnetic susceptibility of $LaCoO_3$. The second transition from insulator to metal has been interpreted as a transition from localized to delocalized e_g bands.[12] Neutron diffraction data show that $LaCoO_3$ undergoes anomalous thermal expansion resulting from the magnetic transitions.[22] Consensus regarding the Co^{3+} spin state in $LaCoO_3$ above 90 K remains elusive.

Numerous theoretical studies have attempted to solidify consensus regarding the relevant spin states of the Co^{3+} ions. Unfortunately, Kohn-Sham density functional theory (DFT), within either the local density approximation (LDA) or generalized-gradient approximation (GGA) treatment of electron exchange and correlation, generally fails to properly describe LS $LaCoO_3$ (predicting metallic instead of insulating behavior).[23,24] Therefore, many studies have employed the DFT+U method to investigate the electronic and magnetic structure of $LaCoO_3$.[25–31] The DFT+U method requires a parameter U_{eff}=U-J that represents the difference between the spherically averaged Coulomb (U) and exchange (J) interactions for electrons of a specified angular momentum (*d* electrons in this case) on the same site (each Co ion in this case). Knížek and coworkers, using a U_{eff} = 5.4 eV, showed that the IS state becomes favored over the low spin state in $LaCoO_3$ as the lattice expands.[26] The same authors later chose U_{eff} = 2.7 eV to show that a mixed HS/LS state was more stable than the IS state.[27,32] These contradictory results demonstrate that

different U_{eff} parameters lead to different conclusions. A more desirable first-principles description of $LaCoO_3$ requires an unbiased choice of U_{eff}, such as a U_{eff} determined from *ab initio* calculations that exactly account for the Coulomb and exchange interactions between *d* electrons on a single Co^{3+} site. Multiple studies have employed U_{eff} values derived from the linear-response method[33] to study multiple spin configurations of $LaCoO_3$.[28–30] Laref *et al.,*[30] used this approach to determine that U_{eff} depends on the Co^{3+} spin state with the values of $U_{eff,LS}$=7.22 eV, $U_{eff,IS}$=7.05 eV and $U_{eff,HS}$=6.65 eV. They conclude that the first magnetic transition involves populating the IS state within a matrix of LS Co^{3+} ions. A theoretically predicted low energy LS-IS transition agrees with earlier studies using large U_{eff} values (U_{eff}>5 eV) but contradicts the results obtained with lower U_{eff} values. Hybrid DFT calculations have been used to understand the electronic structure[34,35] and oxygen vacancy formation energy[36,37] in $LaCoO_3$. However, the computational expense of the hybrid functionals renders them unfeasible for modeling larger supercells required to study oxygen transport in $LaCoO_3$. Beyond DFT and DFT+U supercell model studies, Hozoi *et al.* used an embedded cluster model with multi-reference singles and doubles configuration interaction used to treat the cluster and an embedding potential derived from periodic Hartree-Fock calculations of LS $LaCoO_3$.[38] This study investigated the spin states of Co in the cluster and found a spin-state ordering of LS < HS < IS. However, the small cluster size and the embedding potential imposed an artificial constraint whereby only local excitations to the IS and HS states within a LS background were modeled. In summary, standard DFT calculations fail catastrophically for $LaCoO_3$, DFT+U calculations reach different conclusions depending on the U_{eff} parameter chosen, and the embedded calculations fail to account for long-range distortions which may affect the relative stability of different spin states.

No consensus exists regarding the relevant spin states of Co^{3+} above 90 K. Nonetheless, many experimental and theoretical investigations have addressed oxygen transport in $LaCoO_3$. Experiments show that $LaCoO_3$ has higher oxygen diffusivity than other common $LaMO_3$ perovskites (M=Mn,Fe).[39–41] Oxygen diffusion in $LaCoO_3$ occurs via a vacancy-mediated hopping mechanism.[41] This mechanism gives rise to a diffusion coefficient that is the product of two quantities: the vacancy concentration and the

vacancy diffusion coefficient.[42] The free energy of oxygen vacancy formation ($\Delta G_{f,vac}$) determines the oxygen vacancy concentration (C_v). The vacancy diffusion coefficient (D_v) takes an Arrhenius form with the activation energy determined from the enthalpic barrier (ΔH_{mig}) to the hopping process. Therefore, the overall diffusion coefficient depends on the $\Delta G_{f,vac}$ and ΔH_{mig}. Experimental data provide an overall description of oxygen diffusion in $LaCoO_3$; however, rational design of materials based on $LaCoO_3$ requires understanding the fundamental physics that govern the oxygen transport process. Theoretical studies (using DFT+U calculations) have addressed oxygen vacancy formation in $LaCoO_3$.[36,37,43–46] Recently, Mastrikov *et al.* computed the vacancy formation enthalpy and migration enthalpy in IS $LaCoO_3$ using a 40-atom supercell model and found that their calculated barrier agreed well with the experimentally observed migration barrier.[45] On the other hand, their oxygen vacancy formation enthalpy (3.64 eV) is significantly higher than the experimental oxygen vacancy formation enthalpy (2.17 eV). These significant deviations from experiment mean that oxygen diffusion constants derived from these theoretical data will not be accurate. Hong, *et al.*, addressed O_2 surface exchange kinetics on $LaCoO_3$ and used DFT+U and hybrid DFT calculations to investigate how the Co spin state affects the oxygen vacancy formation energy.[37] These authors find that larger Co^{3+} magnetic moments lead to lower oxygen vacancy formation energies, in contrast to what we find and argue for here (*vide infra*). They attribute the trends in the oxygen vacancy formation energies to changes in the O 2*p* band center, which they use as a descriptor of the Co-O bond strength. This finding, the first to address the impact of Co spin state on oxygen vacancy formation, underscores the need for more refined understanding of the oxygen defect chemistry in $LaCoO_3$, while the migration barrier should also be analyzed considering additional spin states of the Co^{3+} ion.

We have just explained the controversy regarding the spin state of Co^{3+} in $LaCoO_3$ and reviewed literature that provides some atomic-level insight into oxygen diffusion in $LaCoO_3$. Experiments and theory fail to conclusively find that one magnetic configuration of $LaCoO_3$ dominates above 90 K. In fact, experimentalists have found that invoking a mixture of LS, IS, and HS Co^{3+} ions is necessary to

explain the anomalous thermal expansion seen in $LaCoO_3$.[22] Additionally, Raman spectroscopy[37] indicates that all three configurations coexist above 90 K. This insight proves that any conclusive description of physical processes in $LaCoO_3$ must account for a variety of Co^{3+} spin states.

We present an *ab initio* DFT+U study of oxygen transport in $LaCoO_3$ that focuses on the effects of different spin states of Co^{3+}. As explained below, we determine a unique and unbiased *ab initio* value of U_{eff} for Co^{3+} using the method of Mosey, Liao, and Carter.[47] We apply the DFT+U method to four magnetic configurations of $LaCoO_3$: LS, IS, HS and a 1:1 mixture of HS and LS. We analyze the effects of different spin states on the crystal structure, electronic structure, oxygen vacancy formation, and oxygen migration in $LaCoO_3$. Our results show that the oxygen diffusion coefficient depends significantly on the magnetic configuration of $LaCoO_3$. From these results, we provide insights into how to rationally design materials based on $LaCoO_3$.

METHODS AND COMPUTATIONAL DETAILS

The *ab initio* value of U_{eff} for Co^{3+} was determined from unrestricted Hartree-Fock (UHF) calculations on clusters carved out of a Co_3O_4 crystal, embedded in a point charge array according to the method described in ref. [47] using the GAMESS software package.[48,49] This method involves first evaluating the Coulomb and exchange integrals between UHF molecular orbitals and then taking a weighted average of these integrals based on the extent to which *d* orbitals on the central ion (here one of the octahedrally coordinated Co^{3+} ions) contribute to the specific MOs. The weights were determined by Mulliken population analysis[50] as implemented in GAMESS. Therefore, this U_{eff} value is determined without experimental input (apart from the experimental crystal structure used for the embedded cluster). The Stuttgart effective core potential[51] (ECP) for O and the large-core Hay-Wadt ECP[52] for Co (which subsume two and 18 core electrons, respectively) along with the corresponding double-zeta basis sets for the valence electrons were employed. UHF calculations were performed on cluster models (figure 1) of Co_3O_4 in its spinel structure,[53] which were electrostatically embedded using a point charge array

containing more than 6800 point charges. Formal charges were used to assign +2, +3 and –2 to the appropriate point charges while those on the boundary of the point charge array were reduced according to Evjen's method.[54] The clusters were capped with Al^{3+} and Mg^{2+} Hay-Wadt ECPs[55] (where the Al^{3+} ECPs replace Co^{3+} ions and the Mg^{2+} ECPs replace Co^{2+} ions). Al^{3+} and Mg^{2+} were chosen to replace capping Co^{3+} and Co^{2+} ions, respectively, because the ionic radii of the corresponding species are nearly identical.[56] No basis functions were centered on the capping ECPs so these ECPs only provide Pauli repulsion to prevent unphysical leaking of electron density into the point-charge array. UHF calculations were converged such that all clusters up to $Co_{13}O_{38}^{43-}$ had an energy change less than 0.1 μHa. We converged the two largest clusters to an energy change no larger than 22 μHa. While these clusters are highly charged, all cluster calculations were performed on cationic clusters because of the capping ECPs. The central Co ion remains positively charged throughout the calculations, having a Mulliken charge of +1.35 in the CoO_6^{9-} and +1.15 in the $Co_{26}O_{68}^{68-}$ cluster.

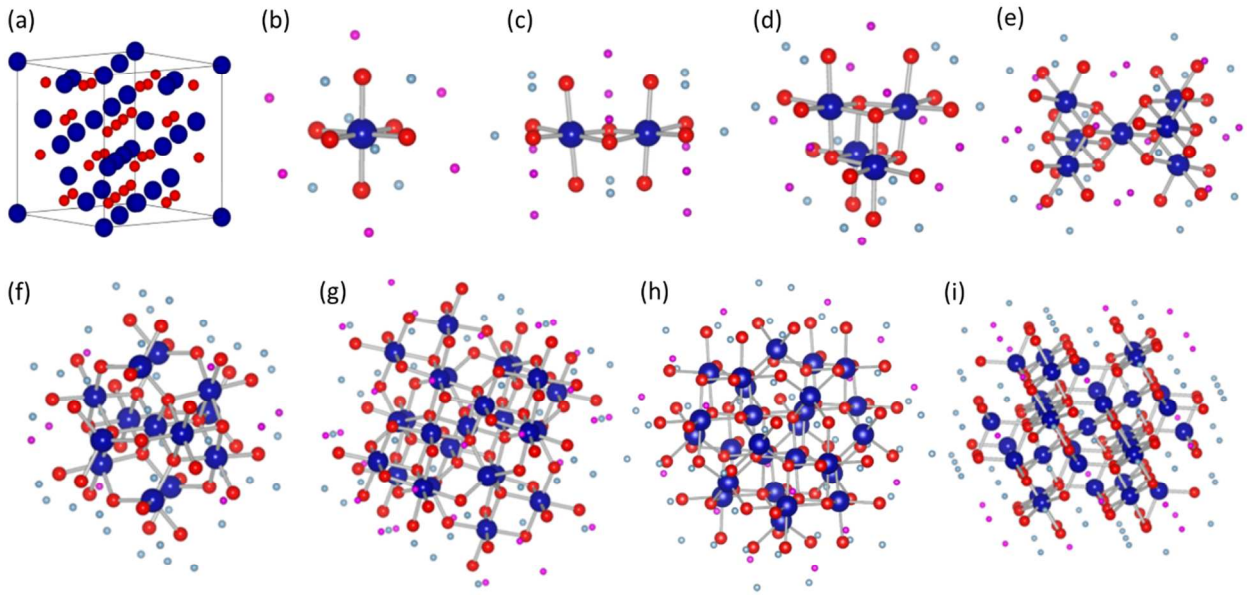

Figure 1. Clusters of Co_3O_4 used in the calculation of U, J and U-J. (a) Co_3O_4 $F\bar{4}3m$ unit cell, (b) CoO_6^{9-}, (c) $Co_2O_{10}^{14-}$, (d) $Co_4O_{16}^{20-}$, (e) $Co_7O_{26}^{31-}$, (f) $Co_{13}O_{38}^{43-}$, (g) $Co_{25}O_{68}^{67-}$, (h) $Co_{26}O_{68}^{68-}$, and (i) $Co_{33}O_{86}^{87-}$. Color designations: Co (blue), O (red), Mg^{2+} capping ECP (pink) and Al^{3+} capping ECP (light blue).

Different structural models were needed to capture the different spin states and observables for $LaCoO_3$. Two cells were employed to describe the bulk crystal and electronic structure of $LaCoO_3$: the $R\bar{3}c$ unit cell (figure 2a) for the LS state and the I2/a cell (figure 2b) for the IS, HS, and LS/HS states. The LS state cannot undergo a JT distortion, so the standard $R\bar{3}c$ unit cell can be used. However, the IS, HS, and HS/LS states may demonstrate JT distortions, so the I2/a cell was chosen to accommodate this possibility. Calculating oxygen vacancy formation energies and oxygen migration pathways required larger cells, so the pseudocubic supercell (40 atoms, figure 2c) and the $2\times2\times2$ $R\bar{3}c$ supercell (80 atoms, figure 2d) were employed. For the supercells, we allowed the atomic coordinates to break symmetry allowing for some stabilization from JT distortions.

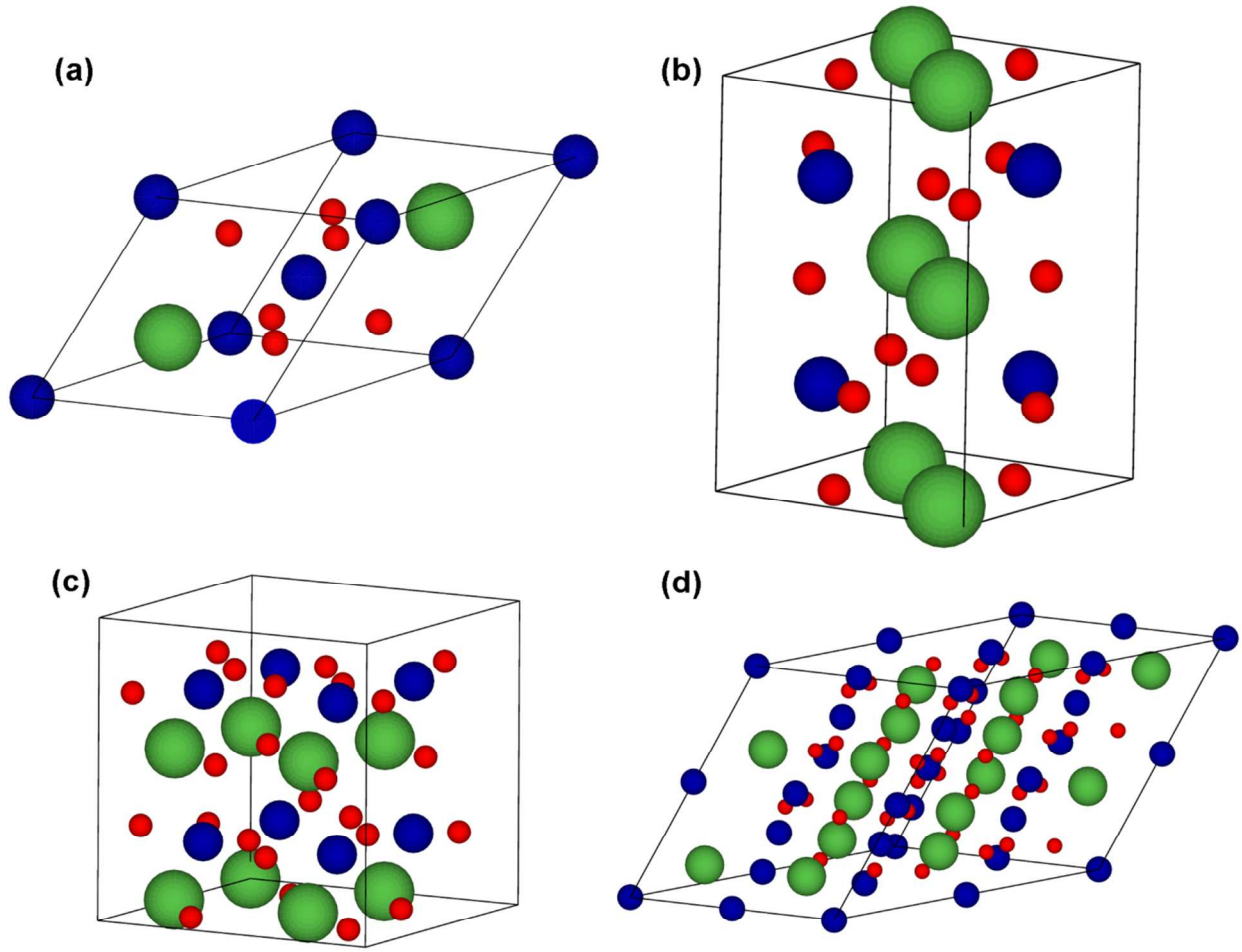

Figure 2. (a) Rhombohedral and (b) monoclinic unit cells of $LaCoO_3$. (c) Pseudocubic and (d) 2×2×2 rhombohedral supercells used for oxygen vacancy calculations in $LaCoO_3$. Color designations: La (green), Co (blue) and O (red).

Kohn-Sham DFT calculations[57,58] with periodic boundary conditions were performed with the Vienna ab initio Simulation Package (VASP) version 5.2.2.[59–61] The nuclei and core electrons were represented within the projector-augmented wave (PAW) formalism.[62] We used standard potentials from the VASP library[63] with the following valence configurations: La ($5s^25p^66s^25d^1$), Co ($4s^23d^7$) and 'regular' O ($2s^22p^4$). Integration over the first Brillouin zone was performed with Gaussian smearing (σ=0.05 eV) on a 4×4×4 Monkhorst-Pack[64] *k*-point mesh for the 10-atom $R\bar{3}c$ unit cell of $LaCoO_3$. A 3×3×2 *k*-point mesh was used for the 20-atom I2/a unit cell, and a 2×2×2 k-point mesh was used for the

40-atom pseudocubic cell and 80-atom rhombohedral supercell (a 2×2×2 supercell of the $R\bar{3}c$ unit cell). The planewave basis set was truncated at 750 eV. Total energies were converged to within 1 meV/atom using these parameters. Electron exchange and correlation was treated with the local density approximation (LDA) and the generalized gradient approximation (GGA) of Perdew, Burke, and Ernzerhof (PBE).[65] LDA+U and GGA+U calculations were performed using the rotationally invariant scheme of Dudarev, *et al*.[66] We compare the performance of LDA+U and GGA+U calculations, noting which predictions are most meaningful in light of their ability to reproduce known observables. Since the DFT+U approach can exhibit metastable states,[67] we carefully examined the initial and final states of our calculations to ensure that comparisons between LDA+U and GGA+U were made between equivalent minima. Each magnetic state was constructed through varying the initial guess for the Co magnetic moments (LS=0, IS=±2, HS=±4, where this quantity is the difference between alpha and beta electrons on a given site). Oxygen migration pathways were determined using the climbing-image nudged elastic band (CINEB) method[68–70] as implemented in the VASP transition state theory tools developed at the University of Texas (http://theory.cm.utexas.edu/vtsttools/). Structures and migration pathways were optimized until the force on each atom fell below 0.03 eV/Å. Vibrational frequencies were obtained by constructing the Hessian matrix (second derivatives of total energy with respect to ion positions) using finite displacements of atoms (0.02 Å displacements). For the larger supercells, we constructed a subset of the Hessian consisting of groups of atoms surrounding the oxygen vacancy or migration pathway.[71]

We employed several tools for analyzing the electronic structure of $LaCoO_3$ in multiple spin states and the absence or presence of an oxygen vacancy. Atom- and angular-momentum-projected densities of states (PDOS) were obtained from single-point calculations using the tetrahedron method with Blöchl corrections.[72] For convenience, PDOS plots show positive values for the majority spin states and negative values for the minority spin states. All PDOS plots were shifted such that the Fermi energy (the energy above which there are no occupied states) equals zero. We also used Bader's atoms in molecules[73] approach, as implemented by Professor Henkelman's group at the University of Texas,[74,75] to partition the electron density in our calculations. Density difference plots showing how electrons

rearrange upon oxygen vacancy formation require a reference density for the oxygen atom. For this purpose, we computed the oxygen atom in a triplet state, but we allowed the minority electron to fractionally occupy the three p-orbitals to obtain a spherical charge density. This is required so that we do not bias our density difference plots through an arbitrary choice of x, y, or z for the doubly occupied 2p orbital. Finally, the magnetic moments we report were obtained by integrating the spin density within a sphere around each atom. The radii for the spheres were determined for each element by the PAW potentials we used (*vide supra*).

RESULTS AND DISCUSSION

Determining U_{eff} for Co^{3+}

Conclusions drawn from previous DFT+U studies of $LaCoO_3$ have depended strongly on the chosen value of the U_{eff} parameter (*vide supra*). For less empirical predictions, we determine the *ab initio* value of U_{eff} for Co^{3+} from UHF calculations on embedded cluster models of Co_3O_4. We choose Co_3O_4 (spinel structure), the simplest cobalt oxide that contains Co^{3+} ions, to give us the most transferable U_{eff} value for Co^{3+} ions in an oxide material. While the U_{eff} value in principle depends on structure and magnetic state, we require a consistent U_{eff} value so that energy differences are valid (*i.e.,* derived from the same Hamiltonian). The U_{eff} value for LS Co^{3+} is most appropriate since it represents the ground state of $LaCoO_3$ and Co_3O_4. Furthermore, at low temperature (T < 5 K), the Co^{3+}-O^{2-} distances are 1.93 Å and 1.91 Å for $LaCoO_3$ and Co_3O_4, respectively. The spinel structure (Co_3O_4) also features tetrahedrally coordinated HS Co^{2+} ions. These Co^{2+} ions align antiferromagnetically with one another.[53,76] The greatest discrepancies between Co_3O_4 and $LaCoO_3$ are the presence of Co^{2+} in Co_3O_4 and the different octahedral linkage in the spinel (edge shared) and perovskite (corner shared) structures. We calculate the values of U, J, and U_{eff}=U-J among the *d* electrons on the central Co^{3+} ion in the cluster. With expanding cluster size, the central Co ion should become increasingly bulk-like. We find (figure 3) that U_{eff}

converges to 4.0 eV in a cluster of $Co_{33}O_{86}^{87-}$. Our result agrees reasonably well with the value U=5 eV obtained for LS Co^{3+} in $LaCoO_3$ by fitting X-ray photoemission data with a parameterized configuration interaction model for a CoO_6 cluster.[77] Likewise, our U_{eff} value is reasonable when compared with the values for other 3+ transition metal ions: Cr^{3+} = 3.2 eV, Fe^{3+} = 4.3 eV.[47] Our U_{eff} value for Co^{3+} disagrees significantly with the values obtained from linear-response theory which are 6.7 eV for LS Co^{3+} in Co_3O_4[78] and 7.22 eV for LS Co^{3+} in $LaCoO_3$.[30] Another linear-response study obtains the U_{eff} value for LS Co^{3+} as a function of structure, giving rise to unreasonable values in excess of 8 eV.[28] Based on this, it seems that linear-response theory can overestimate U_{eff}. This may arise because the linear-response method of calculating U_{eff} derives the self-interaction error correction using a theory (DFT-LDA) which already contains self-interaction error. Thus results from those calculations should be interpreted with caution.

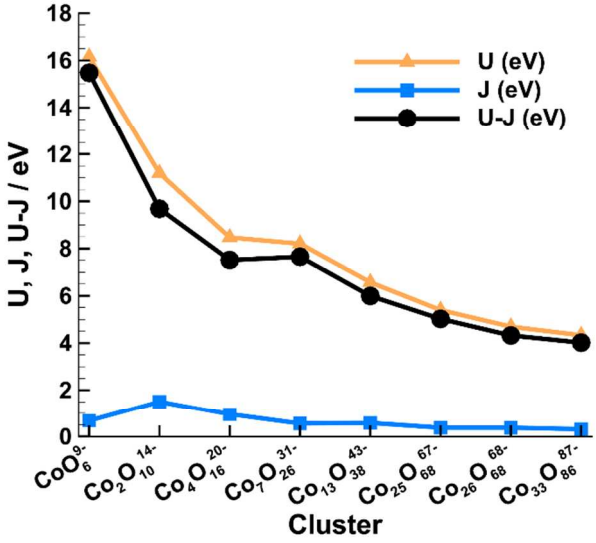

Figure 3. U (orange), J (blue) and U-J (black) for Co^{3+} ions in clusters obtained from Co_3O_4. The converged value of U-J is 4.0 eV. This value is converged to 0.3 eV (the difference between the $Co_{26}O_{68}^{68-}$ and $Co_{33}O_{86}^{87-}$ clusters).

Bulk Structural and Electronic Properties of $LaCoO_3$

To validate the transferability of our *ab initio* U_{eff} value for Co^{3+} from Co_3O_4 to $LaCoO_3$,, we compare experimental observables to those from LDA+U and GGA+U calculations for different Co^{3+}

spin configurations (table 1). We find that the IS state only exists in a ferromagnetic (FM) configuration while the HS state only converges in the antiferromagnetic (AFM) configuration. This may explain why the IS state is routinely found when researchers perform FM DFT+U calculations on $LaCoO_3$.[25,26] Although FM and AFM solutions exist for the HS/LS configuration of $LaCoO_3$, we use an AFM model for this state (in keeping with the paramagnetism of $LaCoO_3$ above 90 K). We require that LS Co^{3+} ions have HS Co^{3+} neighbors (and vice versa) with the HS Co^{3+} aligned antiferromagnetically with one another. Periodic boundary conditions necessitate imposing such order to model a paramagnetic material. Experimental quantities obtained at low temperature (T < 90 K) should be compared to the LS state while observables obtained at room temperature (or higher) should be compared with the magnetic states. As expected, the LDA+U functional gives equilibrium volumes (V_o) smaller than the experimental volumes while the GGA+U functional gives volumes larger than experiment. The optimized lattice constants for both of these functionals follow the same trend as the equilibrium volume. The only exception is the LS case where both functionals underestimate the lattice constant. The GGA+U functional slightly overestimates the LS equilibrium volume because it overestimates the angle between the lattice vectors (61.3^o compared to 61.0^o from experiment)[22] while the LDA+U angle (61.1^o) is in better agreement with experiment. However, neither functional offers a significant advantage in terms of structural parameters. The GGA+U functional gives bulk moduli (B_o) in agreement with room temperature experiments (comparing IS, HS, and HS/LS with experiment) while the LDA+U values are much higher. Finally, the eigenvalue gap between the highest occupied band and the lowest unoccupied band (E_g), which provides a crude estimate of the band gap, is larger than the experimental gap (0.6 eV from optical spectroscopy[79] and 0.9 eV from soft X-ray absorption spectroscopy[80]); however, the eigenvalue gap is close enough that we can reasonably trust both our LDA+U and GGA+U calculations for $LaCoO_3$. Note that the IS state is predicted to be metallic, indicating that it does not play a significant role in the electronic structure of $LaCoO_3$ at temperatures below 500 K (below which $LaCoO_3$ is an insulator). A detailed discussion of the spin state energetics is provided later (*vide infra*). These results suggest that our DFT+U calculations properly capture the physics of $LaCoO_3$.

Table 1. Equilibrium volumes per formula unit, f.u.(V_0), lattice constants (a, b, c), bulk moduli (B_0), and eigenvalue gaps (E_g) of $LaCoO_3$ in different spin states calculated with LDA+U and GGA+U using the *ab initio* value U_{eff}=4.0 eV, as compared with experiment. V_0 and a values for LS $LaCoO_3$ should be compared to the 5 K value while the IS, HS/LS, and HS states should be compared with the 295 K value. The LS (5 K) structure is rhombohedral and requires only one lattice constant (a). The IS, HS/LS, and HS states were analyzed in the monoclinic cell which has three separate lattice constants (a, b, and c). B_0 and E_g measurements were conducted at room temperature; therefore these properties should be compared only to IS, HS/LS, and HS state predictions.

		LDA+U				GGA+U			
Property	**Experiment**	**LS**	**IS (FM)**	**HS/LS**	**HS (AFM)**	**LS**	**IS (FM)**	**HS/LS**	**HS (AFM)**
V_0	55.21 (5 K)[a]	52.32				56.50			
(Å^3/f.u.)	55.71 (295 K)[b]		53.96	53.82	55.61		58.97	58.25	60.12
a / Å	5.426 (5 K)[a]	5.246				5.375			
	5.370 (295 K)[b]		5.312	5.350	5.304		5.476	5.418	5.416
b / Å	----	----				----			
	5.433 (295 K)[b]		5.345	5.391	5.466		5.554	5.506	5.585
c / Å	----	----				----			
	7.640 (295 K)[b]		7.605	7.466	7.678		7.759	7.813	7.952
B_0 (GPa)	120[c], 150[d]	222	203	206	195	177	149	157	152
E_g (eV)	0.6[e], 0.9[f]	0.87	Metal	1.05	1.08	1.12	Metal	1.14	1.46

[a] Ref. 22
[b] Ref. 19
[c] Ref. 11
[d] Ref. 81 at room temperature
[e] Ref. 79: optical gap
[f] Ref. 80: gap from soft X-ray absorption at room temperature

Having validated our *ab initio* DFT+U method against measured bulk properties of $LaCoO_3$, we now consider how the spin state of Co affects the electronic structure of $LaCoO_3$ using Bader analysis[73–75] (table 2) and PDOS (figure 4). First, the Bader charge on La (q_{La}) shows negligible variation with the magnetic configuration, indicating that the significant interactions occur between the other atoms (Co and O). Bader analysis reveals that q_{Co} becomes significantly more positive with increasing magnetic moment on the Co ion. Correspondingly, q_O becomes more negative as μ_{Co} increases. These trends indicate that the system becomes increasingly ionic for higher μ_{Co}. This is also consistent with the fact that the HS state has the largest eigenvalue gap (table 1), suggesting that it is the most ionic. Analyzing the PDOS reveals strong hybridization of Co 3*d* and O 2*p* states in all spin states, based on their overlapping energies. Consistent with a diamagnetic state, the LS PDOS is perfectly symmetrical with regard to majority and minority spin states, and the Co 3*d* states contribute to both the valence and conduction

bands. This result agrees with the crystal field picture of LS $LaCoO_3$ in which Co^{3+} has a $t_{2g}^6 e_g^0$ electron configuration. The IS state is half-metallic with a wide Co 3*d* band crossing the Fermi level in the majority spin states. This delocalization is consistent with the $t_{2g}^5 e_g^1$ electron configuration that has a half-filled e_g band. The JT distortion is insufficient to limit the delocalization of the e_g electrons resulting in the metallic state. The HS state of $LaCoO_3$ has all of the majority Co 3*d* states in the valence band (as expected for the $t_{2g}^4 e_g^2$ configuration). The minority Co 3*d* states are very broad in the valence band (consistent with one of three t_{2g} orbitals being occupied). The conduction band has no significant majority spin states and significant minority Co 3*d* peaks indicating that most of the minority Co 3*d* states are unoccupied. The HS/LS configuration shows a convolution of LS and HS states in $LaCoO_3$. Specifically, the large peak at low energy corresponds to the HS Co ions and the increased density of Co 3*d* states at the top of the valence band is consistent with the LS Co ions. Additionally, the conduction band has majority Co 3*d* states (consistent with LS Co ions) and the sharp peak in the minority channel (consistent with HS Co ions). Finally, we note that in all cases, the O 2*p* states fall almost entirely in the valence band, corresponding to their essentially closed-shell character.

Table 2. Magnetic moments (μ_{Co}) and Bader charges (q) of $LaCoO_3$ in different spin states calculated with LDA+U and GGA+U with the *ab initio* value U_{eff}=4.0 eV.

	LDA+U				GGA+U			
Property	**LS**	**IS (FM)**	**HS/LS**	**HS (AFM)**	**LS**	**IS (FM)**	**HS/LS**	**HS (AFM)**
μ_{Co} (μ_B)	0.00	1.94	2.97 HS 0.05 LS	2.88	0.00	2.16	3.04 HS 0.13 LS	2.98
q_{La} (*e*)	2.06	2.05	2.05	2.07	2.09	2.10	2.09	2.09
q_{Co} (*e*)	1.25	1.31	1.47 HS 1.25 LS	1.45	1.30	1.36	1.54 HS 1.30 LS	1.52
q_O (*e*)	-1.10	-1.12	-1.14	-1.17	-1.13	-1.15	-1.17	-1.20

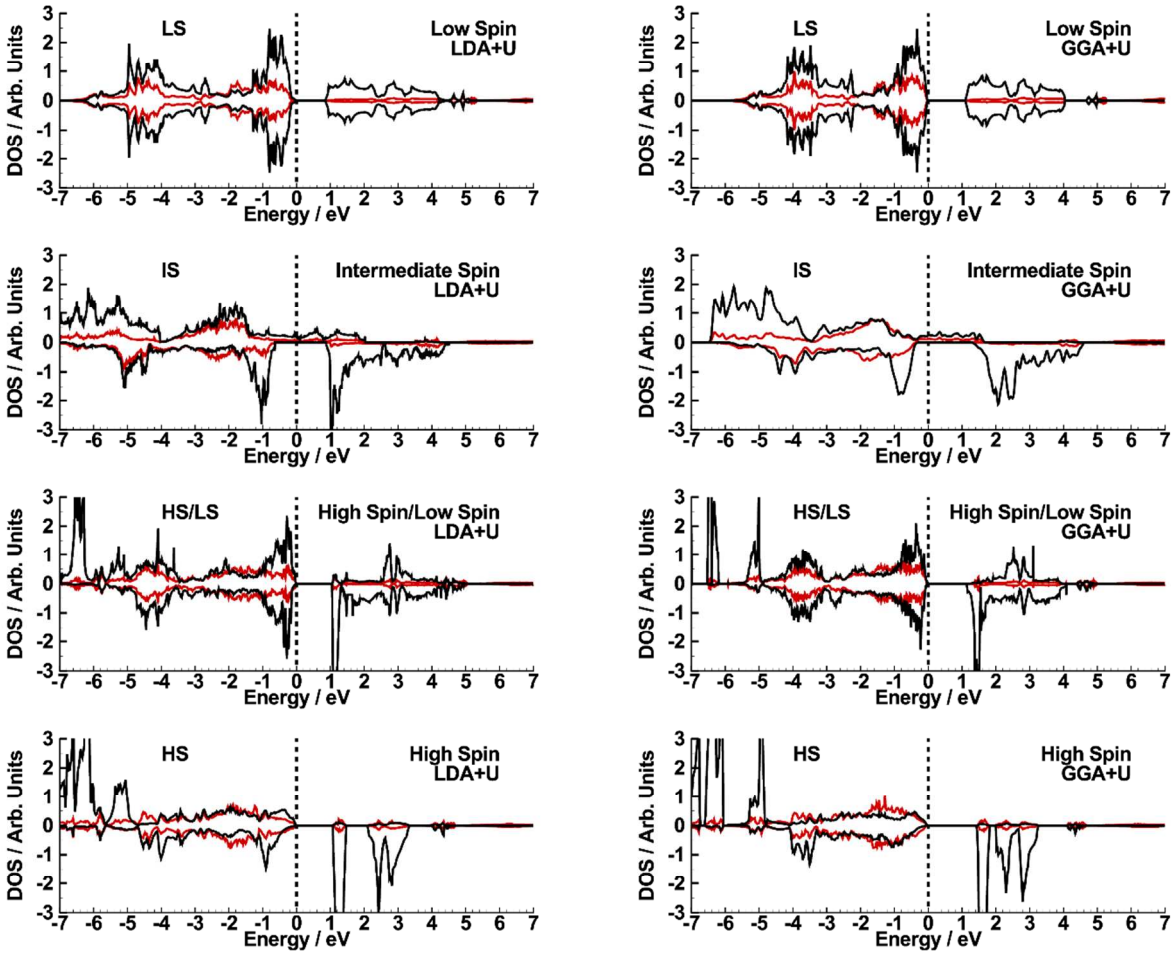

Figure 4. Projected densities of states for $LaCoO_3$ with the Co ions (from top to bottom) in the low spin (LS), intermediate spin (IS), high spin/low spin (HS/LS), and high spin (HS) states with the LDA+U (left) and GGA+U (right) functionals. Positive values indicate majority spin states while negative values indicate minority spin states. Co 3*d* states (black) and O 2*p* states (red). The dashed vertical line appears at the Fermi level, with occupied states at negative energies and unoccupied states at positive energies.

The nature of the transition from nonmagnetic to paramagnetic behavior around 90 K remains controversial, and experiments suggest that a mixture of spin states is responsible for the paramagnetism.[22] To investigate this issue, we computed the equation of state (energy vs. volume, figure 5) for each spin state using LDA+U and GGA+U calculations. We found it sobering that the two sets of calculations give completely opposite qualitative trends. The low spin state (nonmagnetic) is the low temperature ground state and should have the lowest energy among the different spin configurations. LDA+U calculations properly predict this. However, the GGA+U calculations incorrectly predict that the

LS state has the highest equilibrium energy. Finally, our hybrid DFT calculations using the HSE06[82,83] functional indicate that, although this functional mostly uses GGA (PBE) exchange and correlation, the inclusion of short-range exact exchange gives a reasonable ordering of LS < HS. Others have shown that the B3LYP[84] hybrid functional produces a reasonable spin state ordering for $LaCoO_3$.[35] While hybrid functionals offer an alternative to LDA+U for analyzing the ordering of spin states, we believe that significant insight can be gleaned by examining the LDA+U energetics.

When considering which spin states occur above 90 K, we rely on the LDA+U results. We find that an equal mixture of HS and LS Co ions is slightly favored over the IS state. However, the HS/LS mixture and the IS state have similar energies, meaning that both states may contribute to the paramagnetism of $LaCoO_3$. Finally, the HS state lies more than 0.1 eV/f.u. above the mixed HS/LS state indicating that a purely HS state is less stable than a mixture of HS and LS Co^{3+} ions. Overall, LDA+U data, which we believe are more meaningful in this situation, support the notion that the nonmagnetic-to-paramagnetic transition arises from Co^{3+} ions being excited into the HS state within a background that is mostly LS in nature.[27] Since our electronic structure calculations indicate that the IS state is metallic, this latter state most likely only exists above the insulator to metal transition (500 K). The IS and HS/LS spin states probably coexist at SOFC operating temperatures, proving that a thorough analysis of oxygen transport in $LaCoO_3$ must include Co spin state effects.

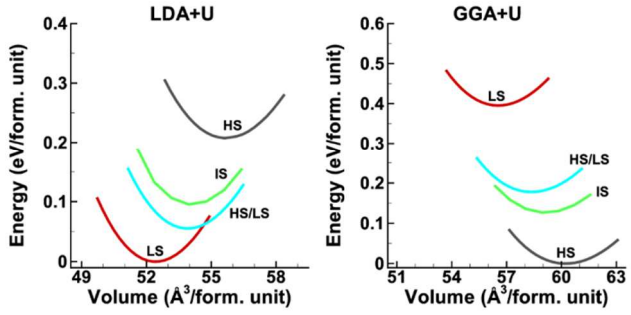

Figure 5. Energy vs. volume for $LaCoO_3$ with different spin states of Co. LDA+U gives (reasonable) LS < HS/LS < IS < HS ordering while GGA+U gives (unreasonable) HS < IS < HS/LS < LS ordering.

Oxygen Diffusion in $LaCoO_3$

Analyzing the effects of different Co spin states on oxygen transport requires understanding the oxygen diffusion mechanism. Experiments show that oxygen diffusion occurs via a vacancy-mediated hopping mechanism.[41,42] Again, when diffusion occurs via this mechanism, two parameters control the oxygen diffusion coefficient (D_O): C_v and D_v (eq. 1).

$$D_O = \frac{C_v}{C_O} D_v = \frac{C_v}{3 - C_V} D_v \quad (1)$$

C_V and C_O are the oxygen vacancy and oxygen concentrations, respectively. We express these quantities in moles/mole $LaCoO_3$. This accounts for the factor of 3 in the denominator of eq. 1. $\Delta G_{f,vac}$ governs C_v (*vide infra*) while D_v adopts an Arrhenius form (eq. 2).

$$D_v = A e^{-\Delta H_{mig}/k_B T} = \frac{1}{6} \upsilon_0 a^2 e^{-\Delta S^{\ddagger}/k_B} e^{-\Delta H_{mig}/k_B T} \quad (2)$$

The righthand side of equation 2 arises from transition state theory[85,86] where υ_0 is the attempt frequency, a is the jump length, $\Delta S^{\ddagger}$ is the entropy difference between the initial and transition states, the factor of 1/6 arises from diffusion in three dimensions, and ΔH_{mig} is the enthalpic barrier to migration. In light of the controversy over the different spin states in $LaCoO_3$ (*vide supra*), our analysis of oxygen transport will show how different Co spin states alter the oxygen vacancy formation process (*e.g.,* $\Delta G_{f,vac}$) and the oxygen migration process (*e.g.,* ΔH_{mig}).

Oxygen vacancies play a fundamental role in the oxygen transport mechanism in $LaCoO_3$ (*vide supra*). We therefore analyze how the magnetic state of Co^{3+} changes the fundamental physics of oxygen vacancy formation. Since experiments indicate that oxygen vacancies interact negligibly with one another in $LaCoO_3$,[41,87] we require a model which reproduces the dilute limit of oxygen vacancies. We first computed $\Delta E_{f,vac}$ (eq. 3), which neglects thermal effects (*vide infra*), in the pseudocubic (40-atom) and 2×2×2 rhombohedral (80-atom) supercells.

$$\Delta E_{f,vac} = E_{defective} - E_{perfect} + \frac{1}{2} E_{O_2} \quad (3)$$

We find that $\Delta E_{f,vac}$ decreases by as much as 0.48 eV when increasing the supercell size from pseudocubic to rhombohedral (table 3). Thus, vacancy-vacancy interactions (arising from periodic boundary conditions) are significant in the pseudocubic cell. We further increased the rhombohedral supercell size from 2×2×2 (80 atoms) to 3×3×3 (270 atoms), and we found that the LDA+U LS oxygen vacancy formation energy decreases by only 0.12 eV. This difference is sufficiently small to show that the 2×2×2 rhombohedral supercell reasonably represents the limit of dilute oxygen vacancies in $LaCoO_3$. The vacancy concentration in this cell is 2.1% (δ=0.0625), which roughly corresponds with the vacancy concentrations determined from thermogravimetry (*e.g.,* $\delta \approx 0.01$ at 950°C and P_{O2} = 0.01 atm).[88] Our larger supercell LDA+U and GGA+U calculations of the vacancy formation energy as a function of spin state (table 3) show that the LS state is the best environment for oxygen vacancy formation. Note that the trends from the 80-atom supercell are reproduced in the pseudocubic 40-atom cell for GGA+U but not for the LDA+U calculations. From this point forward, we ignore the LDA+U oxygen vacancy formation energies because of the well-known overbinding of LDA compared to the GGA, leading to spuriously high vacancy formation energies within LDA+U. As a last point, we predict that the HS state has the highest oxygen vacancy formation energy, and the HS/LS state falls in between these two extremes. This indicates that *changing the operating conditions (e.g., increasing the total pressure should stabilize the LS state, though the oxygen partial pressure should be kept constant to avoid lowering* C_v*)*[81] *or making small modifications to the chemical composition that preserve more LS* Co^{3+} *ions may offer a rational means of increasing the oxygen vacancy concentration (and thus the ionic conductivity) of* $LaCoO_3$*.*

Table 3. Oxygen vacancy formation energy ($\Delta E_{f,vac}$) in $LaCoO_3$ for different Co spin configurations in the pseudocubic and 2×2×2 rhombohedral supercells.

	LDA+U		GGA+U	
Spin State	**Pseudocubic**	**2×2×2 rhombohedral**	**Pseudocubic**	**2×2×2 rhombohedral**
LS	3.27 eV	2.79 eV	1.08 eV	0.90 eV
IS	2.85 eV	----[b]	1.37 eV	----[b]
HS	3.07 eV	2.94 eV	2.23 eV	1.89 eV
HS/LS	----[c]	3.02 eV	----[c]	1.45 eV
Experiment[a]	2.2 eV			

[a] Ref. [88]
[b] We could not obtain the IS state in the 2×2×2 rhombohedral supercell (*vide infra*)
[c] The HS/LS state cannot be constructed with the proper antiferromagnetism in the pseudocubic cell.

Electronic structure analysis offers a way to explain why the oxygen vacancy formation energy changes with magnetic state. When we analyze the electronic structure of LS and HS $LaCoO_3$ in the presence and absence of an oxygen vacancy using the GGA+U results, we find that Co ions adjacent to the vacancy have magnetic moments around 2.5 μ_B (table 4). Additionally, these ions have significantly reduced charges in the presence of an oxygen vacancy, indicating that they accept the electrons released when the vacancy forms. Since two Co ions were bound to the vacant oxygen site, each accepts one electron resulting in a localized reduction from Co^{3+} to Co^{2+} on these sites. We find that, regardless of whether the oxygen vacancy is formed in HS or LS $LaCoO_3$, the final state of these ions is always high spin Co^{2+}. This occurs because the exchange stabilization of aligning the *d* shell in Co^{2+} is greater than the penalty introduced by the crystal field splitting. These effects are nearly balanced in Co^{3+} (leading to the complex magnetic behavior of $LaCoO_3$); however, in Co^{2+} the crystal field splitting is reduced compared to Co^{3+},[16] so the exchange stabilization effect dominates.

Table 4. Magnetic moments (μ_{Co}) and Bader charges (q) in the 2×2×2 rhombohedral supercell before and after the creation of an oxygen vacancy ($V_O^{\bullet\bullet}$) determined using GGA+U calculations with U_{eff} = 4.0 eV. Co* indicates a cobalt ion adjacent to the vacant oxygen site.

	LS		HS/LS		HS	
	Before $V_O^{\bullet\bullet}$	**After $V_O^{\bullet\bullet}$**	**Before $V_O^{\bullet\bullet}$**	**After $V_O^{\bullet\bullet}$**	**Before $V_O^{\bullet\bullet}$**	**After $V_O^{\bullet\bullet}$**
μ_{Co} (μ_B)	0.0-0.1	0.0-0.1	HS: 3.0 LS: 0.0	HS: 3.0 LS: 0.0	3.0	3.0
μ_{Co*} (μ_B)	------	2.6	------	HS: 2.6[a] LS: 1.9	------	2.5
q_{La} (e)	2.09	2.08 ± .01	2.09	2.08	2.10	2.08 ± .01
q_{Co} (e)	1.31	1.30	HS: 1.54 LS: 1.28	HS: 1.53 LS: 1.28	1.52	1.52
q_{Co*} (e)	------	1.20	------	HS: 1.19, 1.29[a] LS: 1.27	------	1.17
q_O (e)	-1.13	-1.15 ± .02	-1.17	-1.17 ± .01	-1.21	-1.21 ± .01

[a] One HS ion adjacent to the oxygen vacancy and another nearby HS ion show reduced magnetic moments and Bader charges.

We can explicitly verify that the final state after oxygen vacancy formation is high spin Co^{2+} by looking at an electron density difference plot that shows how the electrons rearrange upon vacancy formation in LS $LaCoO_3$ (figure 6). Around the Co ions adjacent to the vacancy, we not only see an increase in electron density, we also see a region of decreased electron density. This demonstrates that a

rearrangement occurs in the *d* manifold of the Co ions, as required by the reduction of LS Co^{3+} to HS Co^{2+}. This also explains why LS $LaCoO_3$ is more receptive to oxygen vacancies than HS $LaCoO_3$. The rearrangement in the *d* manifold allows for additional exchange stabilization in LS $LaCoO_3$ that cannot be gained in HS $LaCoO_3$.[36] HS/LS $LaCoO_3$ behaves slightly differently than its magnetically homogenous counterparts. In this state, the HS Co ion adjacent to the vacancy demonstrates the same reduced magnetic moment as occurs in the HS state. Similarly, the LS Co ion adjacent to the vacancy shows an increased magnetic moment of 1.9 μ_B. To compensate for the fact that the LS Co increases its magnetic moment more than the HS Co reduces its magnetic moment, another HS Co (approximately the same distance from the LS Co ion as the first one) also reduces its magnetic moment. Bader analysis indicates that this second HS Co also undergoes reduction (*q* is significantly reduced from 1.53 to 1.29 *e*) while showing that the LS Co ion adjacent to the vacancy does not undergo a reduction (*q* insignificantly changes from 1.28 to 1.27). Taken together, the magnetic moments and Bader charges for HS/LS show that the oxygen vacancy reduces two HS Co^{3+} sites to HS Co^{2+} (only one of the two is adjacent to the oxygen vacancy) while causing a magnetic transition from LS Co^{3+} to IS Co^{3+} for the LS Co^{3+} ion adjacent to the vacancy. This detailed analysis demonstrates that a single description of oxygen vacancy formation in $LaCoO_3$ will not account for significant changes in the oxygen vacancy formation process caused by different Co^{3+} spin states.

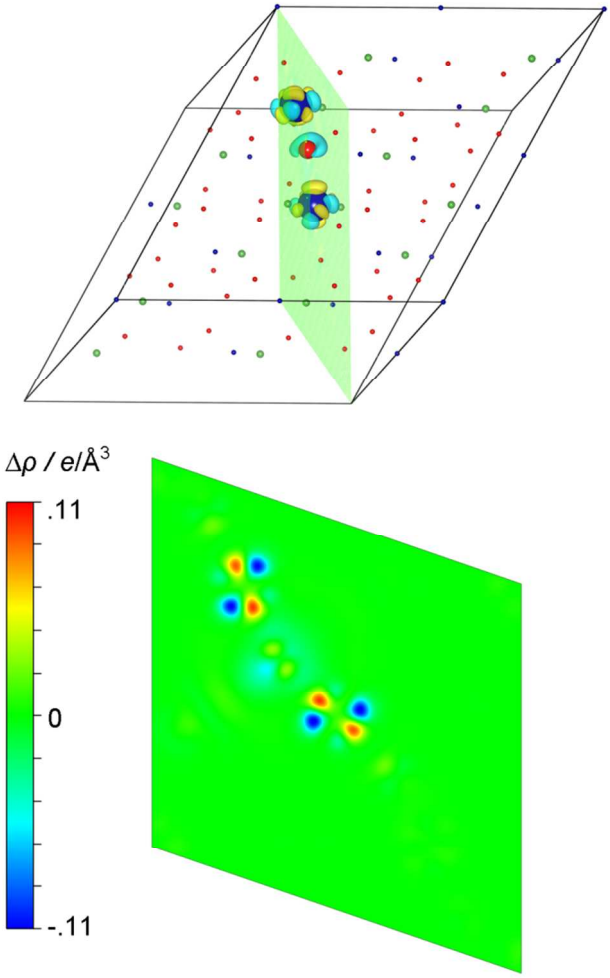

Figure 6. Electron density difference for low spin $LaCoO_3$ ($\Delta\rho = \rho_{defective} + \rho_O - \rho_{host}$) calculated with the GGA+U functional. Volumetric plot (top) with isosurfaces at +0.03 *e*/Å^3 (yellow) and -0.03 *e*/Å^3 (blue). Ions (except those around the vacancy) are shown in reduced size for clarity. Color designations: cobalt (blue), lanthanum (green) and oxygen (red). Contour plot (bottom) on the (211) plane intersecting the oxygen vacancy site and its two nearest Co ions. Figure created with VESTA.[89,90]

Our previous work on $La_{1-x}Sr_xFeO_3$[91] (LSF) demonstrated the relevance of taking into account thermal corrections to the oxygen vacancy formation energy. In agreement with Gryaznov, *et al.*,[92] we found that the thermal contributions from the perfect and defective LSF solids contributed significantly to $\Delta G_{f,vac}$. We expect that $LaCoO_3$ will show similar contributions from the solids, so we provide oxygen vacancy formation energies (table 5) using different levels of approximation for the thermal corrections

(see ref. [91] for equations). The approximations are as follows: $\Delta E_{f,vac}$ neglects all thermal corrections, $\Delta H_{f,vac}$(0 K) includes zero-point energy (ZPE) corrections, $\Delta H_{f,vac}$(700°C) includes ZPE corrections plus the heat capacity (C_p) integrated from absolute zero to 700°C and $\Delta G_{f,vac}$(700°C) includes $\Delta H_{f,vac}$(700°C) and entropic (S) terms. We determined C_p and S for the solid phases by using the harmonic oscillator approximation with the vibrational frequencies determined from a cluster of atoms within the supercell containing the departing oxygen ion and the two cobalt ions around the defect site. We provide an LDA+U and GGA+U analysis of phonon frequencies in LS $LaCoO_3$ in the supporting information. For the solid phases, we neglected PV terms in the enthalpy and assumed that the constant volume heat capacity equals C_p.[93] We chose this cluster for the vibrational frequency calculations based on comparing clusters of increasing size (up to 16 atoms) and seeing that the thermal contributions to the vacancy formation enthalpies and free energies were converged to 0.02 eV for the small cluster. We used the standard ideal gas, rigid rotor, and harmonic oscillator approximations for homonuclear diatomic molecules[93] to determine C_p and S for O_2(g). We account for the PV contribution to the enthalpy of O_2(g) by integrating C_p instead of C_v. The large entropic contribution to $\Delta G_{f,vac}$ arises from the vacancy formation process releasing an oxygen atom from the lattice to form half of an O_2(g) molecule. For $LaCoO_3$, the thermal corrections only make a small impact on the enthalpies of vacancy formation. The significant entropic contribution from the gas-phase O_2 molecule gives rise to large thermal contributions in $\Delta G_{f,vac}$. A correction ($\Delta E = 0.42$ eV) for the known overbinding of O_2 by DFT-GGA was derived by subtracting the experimental O_2 bond dissociation energy from the computed O_2 bond dissociation energy and dividing by 2 (since ½O_2(g) is the product of oxygen vacancy formation). This correction shifts the vacancy formation energies upwards because it destabilizes the products (specifically the ½O_2).

Table 5. Oxygen vacancy formation energies in $LaCoO_3$ for different Co spin states with different approximations to the thermal contributions. Thermal corrections use P_{O_2}= 1 atm for the ideal gas approximation. Calculations performed at the GGA+U level in the 2×2×2 rhombohedral supercell. Values in parentheses reflect a correction for the known overbinding of O_2 by DFT-GGA.

Spin State	$\Delta E_{f,vac}$ / eV	$\Delta H_{f,vac}$(0K) / eV	$\Delta H_{f,vac}$(700°C) / eV	$\Delta G_{f,vac}$(700°C) / eV
LS	0.90 (1.32)	0.85 (1.27)	0.84 (1.26)	-0.08 (0.34)
HS	1.89 (2.31)	1.86 (2.28)	1.83 (2.25)	0.99 (1.41)
HS/LS	1.45 (1.87)	1.44 (1.86)	1.40 (1.82)	0.62 (1.04)
Experiment[88]		2.2		1.2

We do not present the vacancy formation process in IS $LaCoO_3$ because we were unable to stabilize that configuration within the 2×2×2 rhombohedral supercell. This lack of convergence is likely due to the supercell not accommodating the JT distortion required by the IS state. We did obtain the vacancy formation energy for the FM IS state in the pseudocubic supercell, and found it exceeds the LS state value by 0.28 eV (within GGA+U theory in the pseudocubic supercell). Others have also investigated oxygen vacancy formation in IS $LaCoO_3$ in the pseudocubic cell.[43,45,46] Lee, *et al.*[43] employed an optimized U_{eff} value of 3.3 eV for Co^{3+} obtained by fitting the reaction enthalpy for forming $LaCoO_3$ from CoO, La_2O_3, and O_2. Their oxygen vacancy formation energy in the FM IS state, including an empirical correction for the known DFT-GGA overbinding of O_2, is between 2.5 and 3 eV, somewhat higher than experiment. Recently published work by Mastrikov, *et al.*[45,46] used DFT-GGA to calculate the oxygen vacancy formation energy for the IS FM configuration of $LaCoO_3$ in a rhombohedral variant of the 40-atom supercell. Their reported values of $\Delta E_{f,vac}$ = 3.42 eV and 3.64 eV far exceed experiment, and the errors likely result from the well-known misrepresentation of the $LaCoO_3$ electronic structure by DFT-GGA (as opposed to GGA+U or hybrid DFT). Additionally, our results show that the 40-atom supercell they used probably produces a significant overestimation of $\Delta E_{f,vac}$, and larger supercells should be employed to determine whether their value is converged.

As mentioned earlier, Hong, *et al*. examined surface exchange kinetics of $LaCoO_3$ using both experimental methods and DFT-based calculations.[37] As in our present study, they investigated $\Delta E_{f,vac}$ for various Co magnetic moments. In contrast to our study here, they predicted that the LS state would have the highest $\Delta E_{f,vac}$ (~3.5 eV), for both GGA+U and hybrid functional calculations in the 40-atom supercell. Lower $\Delta E_{f,vac}$ values (derived from GGA+U) of ~2.7 eV and ~2.4 eV were reported for the ferromagnetic IS and HS states, respectively. These spin states experienced dramatic decreases in $\Delta E_{f,vac}$ to 1.3 eV and 1.4 eV, respectively, with hybrid functionals. Such large changes are not surprising given the significant differences between our calculations and those of Hong, *et al*. They utilized the 40-atom supercell that we showed to be insufficient for describing oxygen vacancy formation in $LaCoO_3$.

Numerical differences between their work and ours include the U_{eff} value (empirically fit value of 3.3 eV vs. *ab initio* value of 4.0 eV), slightly different GGA functionals (PW-91 vs. PBE), and the use of a lower planewave kinetic energy cutoff (600 eV vs. 750 eV). In order to obtain results for a specific spin state, Hong, *et al.* fixed the overall magnetization of the cell. In contrast, we allow free relaxation of the spin density, only constraining antiferromagnetic solutions to have equal numbers of alpha and beta electrons. Finally, they do not report the magnetization of the final states they obtained for any of the spin states they examined. These differences, especially the last one, may explain some of the differences in our values. Our argument for the reduced vacancy formation energy in the LS state comes from well-founded physical arguments: the extra intra-atomic exchange stabilization gained by the final state relaxing from LS Co^{2+} to HS Co^{2+} lowers the oxygen vacancy formation energy for the low spin state (*vide supra*). Though Hong, *et al.* rely on the O 2*p* band center as a measure of the Co-O bond strength, this metric depends on the methodology (*e.g.*, GGA functional, PAW potential) and does not account for final state relaxations which may lower the cost of breaking the bond. Additionally, the bands provided by DFT are of limited value because they have no physical meaning (in the Kohn-Sham formalism, orbitals or bands are used only as a convenience for evaluating the kinetic energy term and are not unique). Given our use of larger supercells, more accurate numerical parameters, and physical arguments based on *d* orbital occupations and charge reorganization, we expect our predictions to be more reliable than those of Hong, *et al*.

Oxygen vacancy formation energies determine the oxygen vacancy concentration. However, theoretical oxygen vacancy concentrations are rarely reported for SOFC cathode materials.[94] Commonly, a Boltzmann factor is used to compute the vacancy concentration (equation 4).[85,86]

$$\frac{C_{\mathrm{v}}}{3 - C_{\mathrm{v}}} = \exp\left(-\frac{\Delta H_{\mathrm{f,vac}}}{k_{\mathrm{B}} T}\right) \tag{4}$$

C_{v} is the oxygen vacancy concentration (moles/mole $LaCoO_3$), $\Delta H_{\mathrm{f,vac}}$ is the enthalpy of vacancy formation, k_{B} is Boltzmann's constant, and T is the absolute temperature. When employing equation 4 to compute C_{v}, we increase $\Delta H_{\mathrm{f,vac}}$ by 0.42 eV to account for the known overbinding of O_2 by DFT-GGA

(*vide supra*). This expression works well for dilute, non-interacting vacancies in situations where the departing atom is referenced to a solid (*e.g.,* Ni vacancies in NiAl[85]). In our case, forming the vacancy leads to a gaseous product and a large, positive entropy change (eq. 5). We employ Kroger-Vink notation[95] where $V_O^{\bullet\bullet}$ represents an oxygen vacancy, Co_{Co}^{x} and O_O^{x} are Co^{3+} and O^{2-} in the crystal, and the grouping $\left\{Co_{Co}^{/} - V_O^{\bullet\bullet} - Co_{Co}^{/}\right\}$represents a vacancy cluster where two Co^{3+} ions near the vacancy have been reduced to Co^{2+}.

$$2Co_{Co}^{x} + O_O^{x} \rightarrow \left\{Co_{Co}^{/} - V_O^{\bullet\bullet} - Co_{Co}^{/}\right\} + \frac{1}{2}O_2(g) \quad (5)$$

The large entropic change arising from forming O_2(g) necessitates using equilibrium approaches to compute C_v as illustrated in equation 6.[96] Recall that we defined C_v in terms of moles/mole $LaCoO_3$ (*vide supra*).

$$K = \exp\left(-\frac{\Delta G_{f,vac}^{0}}{k_B T}\right) = \frac{\left[\left\{Co_{Co}^{/} - V_O^{\bullet\bullet} - Co_{Co}^{/}\right\}\right]P_{O_2}^{1/2}}{[Co_{Co}^{x}]^2[O_O^{x}]} = \frac{C_v P_{O_2}^{1/2}}{(1-2C_v)^2(3-C_v)} \quad (6)$$

The computed vacancy concentrations using equation 4 (traditional method) and equation 6 (equilibrium method) are shown in figure 7 where the partial pressure of O_2 is 49 torr, corresponding to the experimental conditions.[41] All equilibrium calculations were carried out with 0.42 eV added to $\Delta G_{f,vac}$ to compensate for the known overbinding of the O_2 molecule by DFT-GGA (*vide supra*). *These results confirm our previous assertion that different spin states in $LaCoO_3$ lead to large changes (2-3 orders of magnitude) in oxygen vacancy concentrations.* We also observe that the LS spin state gives the highest oxygen vacancy concentration, in agreement with our reported $\Delta H_{f,vac}$ and $\Delta G_{f,vac}$ values. The traditional method always gives far lower oxygen vacancy concentrations than the equilibrium method because it neglects the positive entropy contribution from the O_2 molecule. The slopes of the LS and HS/LS curves are less negative than the experimental value because the slope is controlled by the enthalpy of vacancy formation (which we underestimate with respect to experiment). The HS curve has a similar slope to the experimental concentration because its adjusted $\Delta H_{f,vac}$ agrees well with experiment. As expected, the

HS/LS and LS results predict C_v values greater than experiment. The HS/LS and HS *C*v curves bracket the experimental curve in agreement with their adjusted $\Delta G_{f,vac}$ values lying below and above, respectively, the experimental value. Physically, a mixture of Co^{3+} spin states contribute to $LaCoO_3$, so a proper comparison between our results and the experimental C_v data is not possible. For example, if the material had more HS than LS Co^{3+} ions, then we would expect the C_v curve to shift downward with respect to the HS/LS curve (toward the experimental values) because the trend is toward lower C_v with increasing HS Co^{3+}. The curves in figure 7 become steeper for larger μ_{Co}, mirroring the trend we found for $\Delta H_{f,vac}$ (the slope is, approximately, $-\Delta H_{f,vac}/k_B$). A valid comparison with experimental C_v data requires larger length/time (*e.g.,* Monte Carlo) simulations that account for thermal population of different Co^{3+} spin states and the effect of magnetic heterogeneity on the oxygen vacancy formation energies. Such simulations are beyond the scope of this work. The trends we find provide sufficient atomic-level insight into how various Co^{3+} spin states affect oxygen transport in $LaCoO_3$. *Our results demonstrate that engineering $LaCoO_3$-based cathode materials to have higher LS Co^{3+} concentrations should improve the oxygen diffusivity of these materials. This effect will be largest for pure $LaCoO_3$.*

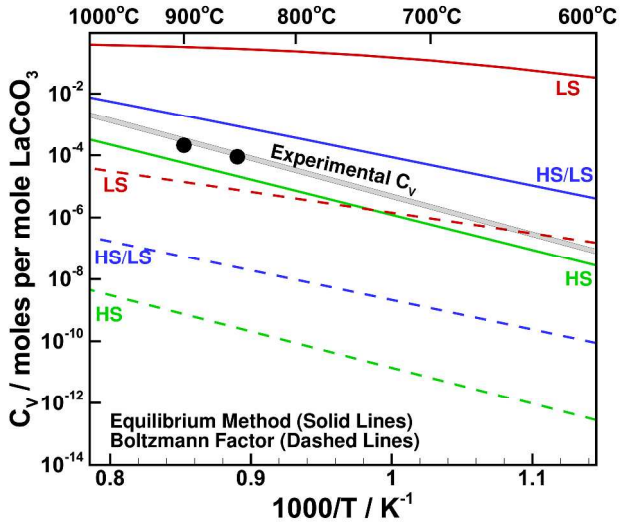

Figure 7. Oxygen vacancy concentrations (C_v, moles per mole $LaCoO_3$) as a function of temperature computed for the LS (red), HS/LS (blue), and HS (green) spin states of $LaCoO_3$. Solid lines use the equilibrium method while dashed lines employ the traditional method as discussed in the text. Experimental data (gray area) from Ishigaki *et al.*[41] where C_v was estimated as the ratio of the vacancy

diffusion coefficient (D_v) to the oxygen tracer diffusion coefficient (D_O^*) multiplied by a constant factor of 1.0 or 0.69.[41,42] Tabulated experimental data points (black circles) from ref. 41.

Our discussion of oxygen vacancy formation in $LaCoO_3$ shows that the Co^{3+} spin state significantly affects the concentration of oxygen vacancies by altering $\Delta G_{f,vac}$. Completely understanding oxygen ion transport in $LaCoO_3$ requires considering how the migration process couples to the magnetic configuration of Co^{3+}. For this purpose, we identified the minimum energy pathways for oxygen migration in the LS and HS/LS states using GGA+U calculations (figure 8). We did not investigate oxygen migration in the HS state because it probably does not occur independently (*vide supra*). Migration in the IS state was previously studied by Mastrikov, *et al*.[45,46] The pathways (parts a and d) show slightly curved behavior consistent with the prediction made by Islam and Jones for $LaFeO_3$.[97] The predicted migration barriers (parts b and e) are 0.69 eV and 0.49 eV for LS and HS/LS $LaCoO_3$ respectively while the experimental migration barrier from tracer diffusion experiments is 0.78 ± 0.22 eV obtained for $700^oC < T < 1000^oC$.[41] Tsvetkov *et al.*[87] obtained 1.08 ± 0.10 eV for the migration barrier using polarization experiments. Tracer diffusion experiments provide a better comparison for our computed barriers because they do not involve an electric potential gradient (present in the polarization experiments). Our calculated barrier for LS $LaCoO_3$ is comparable to the value of 0.71 eV obtained by Mastrikov *et al.*;[45] however, a fair comparison between these theoretical barriers is not possible — their result is for the IS state and our result is for the LS state. Mastrikov *et al*. proposed that higher charge transfer from the migrating O ion to the central B ion at the transition state in (A,A')(B,B')O_3 materials correlates with a lower migration barrier.[45] In agreement with Mastrikov et al.'s finding for IS $LaCoO_3$, we find almost no change in the charge of the migrating oxygen ($\Delta q \leq 0.02\ e$) at the transition state (compared to its charge at the initial state) for both LS and HS/LS $LaCoO_3$. Therefore, although the data presented by Mastrikov, *et al*. show this correlation for $Ba_{1-x}Sr_xCo_{1-y}Fe_yO_3$ (BSCF) and LSCF, this does not explain the difference in the computed barrier heights for LS and HS/LS $LaCoO_3$. In the experimental temperature range, the correct comparison should be between our HS/LS value and the experiment, where

we see our value falls just slightly below the lower end of experimental range. Below we offer insight into this discrepancy.

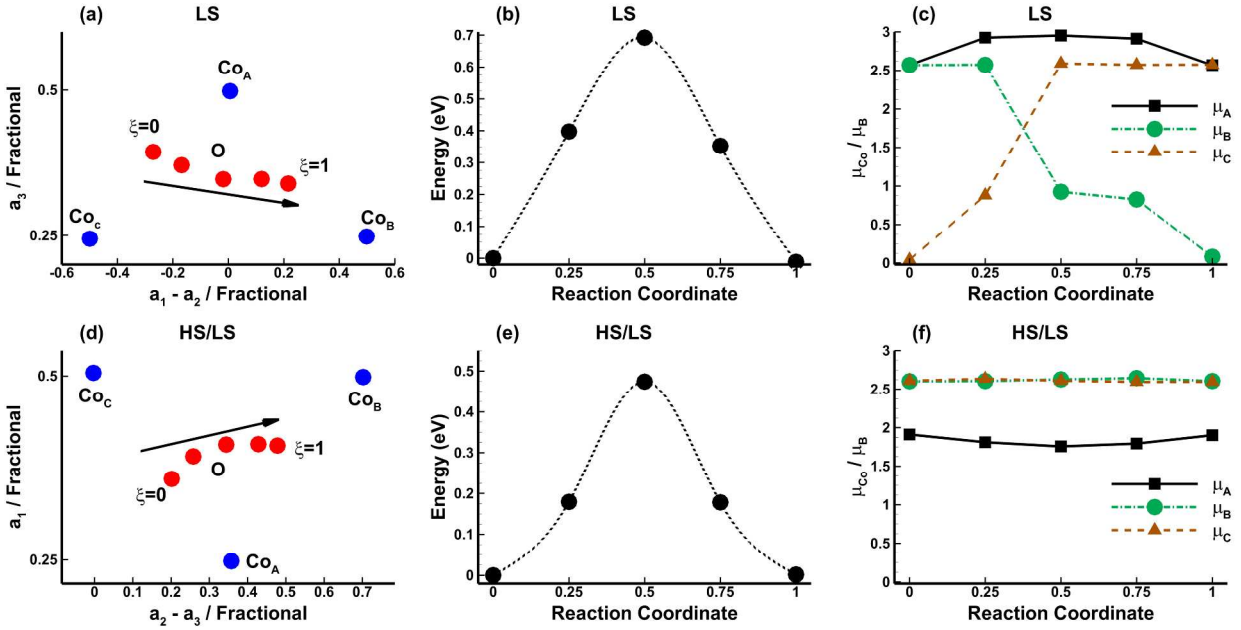

Figure 8. Diffusion pathways, energetics, and magnetism changes for LS and HS/LS $LaCoO_3$. (a) Minimum energy pathway (MEP) for oxygen migration in LS $LaCoO_3$. ξ denotes the reaction coordinate and proceeds from 0 (initial state) to 1 (final state). Co atoms (blue circles) at their nominal positions and O atoms (red circles) at ξ=0, 0.25, 0.50, 0.75, and 1. a_1, a_2, and a_3 refer to the lattice vectors of the 80-atom supercell. (b) Relative energy along the MEP for LS $LaCoO_3$. (c) Co magnetic moments along the MEP for LS $LaCoO_3$. (d) MEP for oxygen migration in HS/LS $LaCoO_3$. (e) Relative energy along the MEP for HS/LS $LaCoO_3$. (f) Co magnetic moments along the MEP for HS/LS $LaCoO_3$.

In addition to obtaining different barriers for LS and HS/LS $LaCoO_3$, we find that the magnetic configuration produces different electronic behavior during oxygen migration. In particular, we see that the magnetic moments of the Co ions surrounding the migration pathway evolve differently in LS than in HS/LS $LaCoO_3$. In LS $LaCoO_3$, oxygen migration involves a magnetic moment crossover between two of the Co ions surrounding the migration pathway (figure 8c). We explain this in terms of an ionic picture. Initially, the vacancy resides between Co_A and Co_B (see figure 8a). This means that Co_A and Co_B exist in a reduced state (HS Co^{2+}) while Co_C remains in the LS Co^{3+} configuration. In the final state, the vacancy resides between Co_A and Co_C, which now exhibit the HS Co^{2+} state while Co_B becomes LS Co^{3+}. Therefore, Co_B is oxidized ($Co^{2+}\rightarrow Co^{3+}$) while Co_C is reduced ($Co^{3+}\rightarrow Co^{2+}$) during the oxygen migration

process. This indicates that the migration process couples to an electron transfer from Co_B to Co_C, which is opposite to the motion of the oxygen ion. We previously demonstrated this same behavior in $LaFeO_3$.[91] HS/LS $LaCoO_3$ does not exhibit this coupling between oxygen ion migration and electron transfer because of the structure of the defect. Our earlier analysis of oxygen vacancy formation in HS/LS $LaCoO_3$ demonstrated that two HS Co^{3+} ions undergo reduction while the LS Co^{3+} ion adjacent to the vacancy becomes IS Co^{3+}. The two HS Co^{3+} (Co_B and Co_C in figure 8d) ions that undergo reduction bracket the diffusion pathway, and their magnetic moments remain essentially constant throughout the migration process. The IS Co^{3+} ion (Co_A in figure 8d) shows a small variation in its magnetic moment along the diffusion pathway, reaching a minimum at the transition state. Because Co_A, Co_B and Co_C bracket the diffusion pathway and their charge/magnetism remains constant throughout the migration (see figure 8(d,f)), no electron transfer couples to the oxygen ion migration in HS/LS $LaCoO_3$. However, in order for long range transport to occur, an electron transfer is required such that two Co^{2+} ions bracket the migration pathway for the next jump. While modeling such an electron transfer is beyond the scope of this article, we expect that accounting for this electron transfer will increase the observed barrier for oxygen migration leading to better agreement with the experimental measurements.

The difference in oxygen migration between HS/LS and LS $LaCoO_3$ is not just an electronic and magnetic issue. The barrier in HS/LS $LaCoO_3$ is significantly lower than in LS $LaCoO_3$ (table 6). To fully analyze the differences between LS and HS/LS $LaCoO_3$, we calculate their oxygen diffusion coefficients using transition state theory. As seen earlier, the calculated barrier for LS $LaCoO_3$ is in reasonable agreement with the experimental data[41] while the calculated barrier for HS/LS $LaCoO_3$ falls below the measured value. Our underestimation of the observed barrier for HS/LS $LaCoO_3$ may result from the inability of our model to include the electron transfer step required to set up the next migration step leading to long range transport as noted above. D_v for LS and HS/LS $LaCoO_3$ are in fair agreement with experiment at 700°C. Since diffusion measurements occur at high temperature, it is of course surprising that the LS state (only stable up to 90 K) shows such good agreement with experiment. We compute the oxygen diffusion coefficient assuming our value of C_v (using eq. 6) and using the

experimental C_v value at 700°C in order to see how these differences affect D_O. The result is a large discrepancy between experiment and theory for the LS state while the agreement is better – though still off - for the HS/LS state. Using the C_v value from experiment, we are nearly within one order of magnitude of experiment. Clearly, the oxygen diffusion coefficient depends strongly on the spin state of the Co^{3+} ions, though primarily through C_v.

Table 6. Diffusion coefficients for LS and HS/LS $LaCoO_3$ calculated with GGA+U.

Parameter	**LS $LaCoO_3$ Calculated**	**HS/LS $LaCoO_3$ Calculated**	**$LaCoO_3$ Experimental**[41]
***a* (Å)**	2.82	2.61	-----
υ_0 (THz)	8.53	6.31	-----
$\Delta S^{\ddagger}/k_B$ [700°C]	-1.86	-2.16	-----
ΔH_{mig} (eV)	0.69	0.47	0.78 ± 0.22
ZPE(TS)–ZPE(Min) (eV)	-0.01	-0.01	-----
***A* (cm^2/s) [700°C]**	7.3×10^{-3}	6.2×10^{-3}	1.59×10^{-2}
D_v (cm^2/s) [700°C]	2.18×10^{-6}	2.58×10^{-5}	1.43×10^{-6}
D_O(cm^2/s) [700°C] (C_v from eq. 6)	3.17×10^{-7}	7.64×10^{-10}	9.20×10^{-13}
D_O(cm^2/s) [700°C] (C_v from expt.)	1.34×10^{-12}	1.58×10^{-11}	

CONCLUSIONS

We have presented an analysis of the effect of Co spin state on oxygen transport in $LaCoO_3$ using detailed first-principles quantum mechanics calculations. Our results provide new understanding regarding the intricacy of $LaCoO_3$, specifically the interrelation of spin state with oxygen ion diffusivity. First, we calculated a new *ab initio* value of $U_{eff} = 4.0$ eV for LS Co^{3+} ions using the method of Mosey, Liao and Carter.[47] We showed how LDA+U and GGA+U calculations lead to different spin state orderings with only LDA+U being reasonable. We then demonstrated that the presence of LS Co^{3+} ions leads to lower oxygen vacancy formation energies. We also showed that the spin state alters the vacancy

migration process and thus the vacancy diffusion coefficient. On the whole, these results confirm that the spin state of the Co^{3+} ions critically influences oxygen transport in $LaCoO_3$.

The results of our study indicate that modifying the operating conditions (*e.g.*, operating pressure) or the material composition (*e.g.*, doping) to increase the number of LS Co^{3+} ions at higher temperatures may offer a route toward improving the ionic conductivity of $LaCoO_3$. The results we provided also form the initial basis for a library of diffusion coefficients, derived from first principles, which can be used for longer time and length scale simulations (*e.g.*, kinetic Monte Carlo). Such an analysis including transitions between spin states, oxygen vacancy formation, and oxygen migration would provide a more complete description of oxygen ion conductivity in $LaCoO_3$.

REFERENCES

1. N. Q. Minh, *Journal of the American Ceramic Society*, 1993, **76**, 563–588.
2. S. B. Adler, *Chem. Rev.*, 2004, **104**, 4791–4844.
3. T. M. Gür, M. Homel, and A. V. Virkar, *J. Power Sources*, 2010, **195**, 1085–1090.
4. M. Homel, T. M. Gür, J. H. Koh, and A. V. Virkar, *J. Power Sources*, 2010, **195**, 6367–6372.
5. E. P. Murray, T. Tsai, and S. A. Barnett, *Nature*, 1999, **400**, 649–651.
6. Z. Lu, J. Hardy, J. Templeton, and J. Stevenson, *J. Power Sources*, 2012, **198**, 90–94.
7. S. . Jiang, *Solid State Ionics*, 2002, **146**, 1–22.
8. S. Stephen J., *International Journal of Inorganic Materials*, 2001, **3**, 113–121.
9. M. Gödickemeier, K. Sasaki, L. J. Gauckler, and I. Riess, *Solid State Ionics*, 1996, **86–88, Part 2**, 691–701.
10. J. M. Ralph, A. C. Schoeler, and M. Krumpelt, *Journal of Materials Science*, 2001, **36**, 1161–1172.
11. J.-S. Zhou, J.-Q. Yan, and J. B. Goodenough, *Phys. Rev. B*, 2005, **71**, 220103.
12. P. M. Raccah and J. B. Goodenough, *J. Appl. Phys.*, 1968, **39**, 1209–1210.
13. M. A. Señarís-Rodríguez and J. B. Goodenough, *J. Solid State Chem.*, 1995, **118**, 323–336.
14. J. Arai, K. Ozawa, and T. Ishiguro, *J. Magn. Magn. Mater.*, 2001, **226–230, Part 1**, 871–873.
15. G. Thornton, B. C. Tofield, and A. W. Hewat, *J. Solid State Chem.*, 1986, **61**, 301–307.
16. P. M. Raccah and J. B. Goodenough, *Phys. Rev.*, 1967, **155**, 932–943.
17. K. Asai, P. Gehring, H. Chou, and G. Shirane, *Phys. Rev. B*, 1989, **40**, 10982–10985.
18. S. Yamaguchi, Y. Okimoto, and Y. Tokura, *Phys. Rev. B*, 1997, **55**, R8666–R8669.
19. G. Maris, Y. Ren, V. Volotchaev, C. Zobel, T. Lorenz, and T. T. M. Palstra, *Phys. Rev. B*, 2003, **67**, 224423.
20. M. W. Haverkort, Z. Hu, J. C. Cezar, T. Burnus, H. Hartmann, M. Reuther, C. Zobel, T. Lorenz, A. Tanaka, N. B. Brookes, H. H. Hsieh, H.-J. Lin, C. T. Chen, and L. H. Tjeng, *Phys. Rev. Lett.*, 2006, **97**, 176405.
21. O. Toulemonde, N. N'Guyen, F. Studer, and A. Traverse, *Journal of Solid State Chemistry*, 2001, **158**, 208–217.
22. P. G. Radaelli and S.-W. Cheong, *Phys. Rev. B*, 2002, **66**, 094408.
23. D. D. Sarma, N. Shanthi, S. R. Barman, N. Hamada, H. Sawada, and K. Terakura, *Phys. Rev. Lett.*, 1995, **75**, 1126–1129.

24. P. Ravindran, P. A. Korzhavyi, H. Fjellvåg, and A. Kjekshus, *Phys. Rev. B*, 1999, **60**, 16423–16434.
25. M. A. Korotin, S. Y. Ezhov, I. V. Solovyev, V. I. Anisimov, D. I. Khomskii, and G. A. Sawatzky, *Phys. Rev. B*, 1996, **54**, 5309–5316.
26. K. Knížek, P. Novák, and Z. Jirák, *Phys. Rev. B*, 2005, **71**, 054420.
27. K. Knížek, Z. Jirák, J. Hejtmánek, P. Novák, and W. Ku, *Phys. Rev. B*, 2009, **79**, 014430.
28. H. Hsu, K. Umemoto, M. Cococcioni, and R. Wentzcovitch, *Phys. Rev. B*, 2009, **79**, 125124.
29. A. Laref and W. Sekkal, *Materials Chemistry and Physics*, 2010, **123**, 125–131.
30. A. Laref, S. Laref, and S. Bin-Omran, *J. Comput. Chem.*, 2012, **33**, 673–684.
31. A. Laref and S. Jun Luo, *Journal of the Physical Society of Japan*, 2010, **79**, 064702.
32. K. Knížek, Z. Jirák, J. Hejtmánek, and P. Novák, *J. Phys.: Condens. Matter*, 2006, **18**, 3285.
33. M. Cococcioni and S. de Gironcoli, *Phys. Rev. B*, 2005, **71**, 035105.
34. D. Gryaznov, R. A. Evarestov, and J. Maier, *Phys. Rev. B*, 2010, **82**, 224301.
35. S. Mukhopadhyay, M. W. Finnis, and N. M. Harrison, *Phys. Rev. B*, 2013, **87**, 125132.
36. M. Pavone, A. M. Ritzmann, and E. A. Carter, *Energy Environ. Sci.*, 2011, **4**, 4933–4937.
37. W. T. Hong, M. Gadre, Y.-L. Lee, M. D. Biegalski, H. M. Christen, D. Morgan, and Y. Shao-Horn, *J. Phys. Chem. Lett.*, 2013, **4**, 2493–2499.
38. L. Hozoi, U. Birkenheuer, H. Stoll, and P. Fulde, *New Journal of Physics*, 2009, **11**, 023023.
39. A. V. Berenov, J. L. MacManus-Driscoll, and J. A. Kilner, *Solid State Ionics*, 1999, **122**, 41–49.
40. T. Ishigaki, S. Yamauchi, J. Mizusaki, K. Fueki, H. Naito, and T. Adachi, *J. Solid State Chem.*, 1984, **55**, 50–53.
41. T. Ishigaki, S. Yamauchi, J. Mizusaki, K. Fueki, and H. Tamura, *Journal of Solid State Chemistry*, 1984, **54**, 100–107.
42. T. Ishigaki, S. Yamauchi, K. Kishio, J. Mizusaki, and K. Fueki, *J. Solid State Chem.*, 1988, **73**, 179–187.
43. Y.-L. Lee, J. Kleis, J. Rossmeisl, and D. Morgan, *Phys. Rev. B*, 2009, **80**, 224101.
44. W. L. Huang, Q. Zhu, W. Ge, and H. Li, *Computational Materials Science*, 2011, **50**, 1800–1805.
45. Y. A. Mastrikov, R. Merkle, E. A. Kotomin, M. M. Kuklja, and J. Maier, *Phys. Chem. Chem. Phys.*, 2013, **15**, 911–918.
46. M. M. Kuklja, E. A. Kotomin, R. Merkle, Y. A. Mastrikov, and J. Maier, *Phys. Chem. Chem. Phys.*, 2013, **15**, 5443–5471.
47. N. J. Mosey, P. Liao, and E. A. Carter, *J. Chem. Phys.*, 2008, **129**, 014103.
48. M. W. Schmidt, K. K. Baldridge, J. A. Boatz, S. T. Elbert, M. S. Gordon, J. H. Jensen, S. Koseki, N. Matsunaga, K. A. Nguyen, S. Su, T. L. Windus, M. Dupuis, and J. A. Montgomery, *J. Comput. Chem.*, 1993, **14**, 1347–1363.
49. M. S. Gordon and M. W. Schmidt, in *Theory and Applications of Computational Chemistry: The First Forty Years*, eds. C. Dykstra, G. Frenking, K. Kim, and G. Scuseria, Elsevier Science, Amsterdam, 1st edn., 2005, pp. 1167–1189.
50. R. S. Mulliken, *The Journal of Chemical Physics*, 1955, **23**, 1833.
51. A. Bergner, M. Dolg, W. Küchle, H. Stoll, and H. Preuß, *Mol. Phys.*, 1993, **80**, 1431–1441.
52. P. J. Hay and W. R. Wadt, *J. Chem. Phys.*, 1985, **82**, 270–283.
53. W. L. Roth, *Journal of Physics and Chemistry of Solids*, 1964, **25**, 1–10.
54. H. M. Evjen, *Phys. Rev.*, 1932, **39**, 675–687.
55. W. R. Wadt and P. J. Hay, *J. Chem. Phys.*, 1985, **82**, 284–298.
56. R. D. Shannon, *Acta Crystallogr. A*, 1976, **32**, 751–767.
57. P. Hohenberg and W. Kohn, *Phys. Rev.*, 1964, **136**, B864–B871.
58. W. Kohn and L. J. Sham, *Phys. Rev.*, 1965, **140**, A1133–A1138.
59. G. Kresse and J. Hafner, *Phys. Rev. B*, 1993, **48**, 13115–13118.
60. G. Kresse and J. Furthmüller, *Phys. Rev. B*, 1996, **54**, 11169–11186.
61. G. Kresse and J. Furthmüller, *Comput. Mater. Sci.*, 1996, **6**, 15–50.

62. P. E. Blöchl, *Phys. Rev. B*, 1994, **50**, 17953–17979.
63. G. Kresse and D. Joubert, *Phys. Rev. B*, 1999, **59**, 1758–1775.
64. H. J. Monkhorst and J. D. Pack, *Phys. Rev. B*, 1976, **13**, 5188–5192.
65. J. P. Perdew, K. Burke, and M. Ernzerhof, *Phys. Rev. Lett.*, 1996, **77**, 3865–3868.
66. S. L. Dudarev, G. A. Botton, S. Y. Savrasov, C. J. Humphreys, and A. P. Sutton, *Phys. Rev. B*, 1998, **57**, 1505–1509.
67. D. Gryaznov, E. Heifets, and E. Kotomin, *Phys. Chem. Chem. Phys.*, 2012, **14**, 4482–4490.
68. H. Jónsson, G. Mills, and K. W. Jacobsen, in *Classical And Quantum Dynamics In Condensed Phase Simulations*, eds. B. J. Berne, G. Ciccotti, and D. F. Coker, World Scientific, Hackensack, NJ, 1998, pp. 385–404.
69. G. Henkelman, B. P. Uberuaga, and H. Jónsson, *J. Chem. Phys.*, 2000, **113**, 9901–9904.
70. G. Henkelman and H. Jónsson, *J. Chem. Phys.*, 2000, **113**, 9978–9985.
71. B. Hinnemann and E. A. Carter, *J. Phys. Chem. C*, 2007, **111**, 7105–7126.
72. P. E. Blöchl, O. Jepsen, and O. K. Andersen, *Phys. Rev. B*, 1994, **49**, 16223–16233.
73. R. F. W. Bader, *Atoms in Molecules: A Quantum Theory*, Oxford University Press, USA, New York, 1994.
74. G. Henkelman, A. Arnaldsson, and H. Jónsson, *Computational Materials Science*, 2006, **36**, 354–360.
75. W. Tang, E. Sanville, and G. Henkelman, *J. Phys.: Condens. Matter*, 2009, **21**, 084204.
76. P. Cossee, *Recl. Trav. Chim. Pay.-B.*, 1956, **75**, 1089–1096.
77. M. Abbate, R. Potze, G. A. Sawatzky, and A. Fujimori, *Phys. Rev. B*, 1994, **49**, 7210–7218.
78. J. Chen and A. Selloni, *Phys. Rev. B*, 2012, **85**, 085306.
79. T. Arima, Y. Tokura, and J. B. Torrance, *Phys. Rev. B*, 1993, **48**, 17006–17009.
80. M. Abbate, J. C. Fuggle, A. Fujimori, L. H. Tjeng, C. T. Chen, R. Potze, G. A. Sawatzky, H. Eisaki, and S. Uchida, *Phys. Rev. B*, 1993, **47**, 16124–16130.
81. T. Vogt, J. A. Hriljac, N. C. Hyatt, and P. Woodward, *Phys. Rev. B*, 2003, **67**, 140401.
82. J. Heyd, G. E. Scuseria, and M. Ernzerhof, *J. Chem. Phys.*, 2003, **118**, 8207–8215.
83. J. Heyd, G. E. Scuseria, and M. Ernzerhof, *J. Chem. Phys.*, 2006, **124**, 219906–219906–1.
84. A. D. Becke, *The Journal of Chemical Physics*, 1993, **98**, 5648–5652.
85. K. A. Marino and E. A. Carter, *Phys. Rev. B*, 2008, **78**, 184105.
86. K. A. Marino and E. A. Carter, *Phys. Rev. B*, 2009, **80**, 069901.
87. D. S. Tsvetkov, A. I. Vylkov, A. Y. Zuev, and A. N. Petrov, *Russ. J. Phys. Chem.*, 2008, **82**, 855–859.
88. J. Mizusaki, Y. Mima, S. Yamauchi, K. Fueki, and H. Tagawa, *J. Solid State Chem.*, 1989, **80**, 102–111.
89. K. Momma and F. Izumi, *J. Appl. Crystallogr.*, 2008, **41**, 653–658.
90. K. Momma and F. Izumi, *Journal of Applied Crystallography*, 2011, **44**, 1272–1276.
91. A. M. Ritzmann, A. B. Muñoz-García, M. Pavone, J. A. Keith, and E. A. Carter, *Chem. Mater.*, 2013, **25**, 3011–3019.
92. D. Gryaznov, M. W. Finnis, R. A. Evarestov, and J. Maier, *Solid State Ionics*, 2014, **254**, 11–16.
93. K. G. Denbigh, *The Principles of Chemical Equilibrium: With Applications in Chemistry and Chemical Engineering*, Cambridge University Press, 4th edn., 1981.
94. A. M. Ritzmann, A. B. Muñoz-García, M. Pavone, J. A. Keith, and E. A. Carter, *MRS Communications*, 2013, **FirstView**, 1–6.
95. F. A. Kröger and H. J. Vink, in *Solid State Physics*, ed. Frederick Seitz and David Turnbull, Academic Press, 1956, vol. Volume 3, pp. 307–435.
96. A. Holt, T. Norby, and R. Glenne, *Ionics*, 1999, **5**, 434–443.
97. A. Jones and M. S. Islam, *J. Phys. Chem. C*, 2008, **112**, 4455–4462.

AUTHOR INFORMATION

Corresponding Author
* Emily A. Carter

Current Address
† John A. Keith, Department of Chemical and Petroleum Engineering, University of Pittsburgh, Pittsburgh, PA 15261, United States

ACKNOWLEDGMENT

The simulations presented in this article were performed (in part) on computational resources supported by the Princeton Institute for Computational Science and Engineering (PICSciE) and the Office of Information Technology's High Performance Computing Center at Princeton University. Part of this research used resources of the National Energy Research Scientific Computing Center, which is supported by the Office of Science of the U.S. Department of Energy under Contract No. DE-AC02-05CH11231. We gratefully acknowledge the computing resources provided on "Fusion," a 320-node computing cluster operated by the Laboratory Computing Resource Center at Argonne National Laboratory. HeteroFoaM, an Energy Frontier Research Center funded by the U.S. Department of Energy, Office of Science, Office of Basic Energy Sciences, under award number DE-SC0001061, supported this work.

TABLE OF CONTENTS GRAPHIC

Caption (20 words, 1 sentence max): Increased low spin Co^{3+} content in $LaCoO_3$ leads to higher oxygen diffusivity by promoting larger oxygen vacancy concentrations.